Single- and multi-doping in graphene quantum dots: unraveling the origin of selectivity in the oxygen reduction reaction

Marco Favaro,[1] *Lara Ferrighi,*[2] *Gianluca Fazio,*[2] *Luciano Colazzo,*[1] *Cristiana Di Valentin,*[2*] *Christian Durante,*[1] *Francesco Sedona,*[1] *Armando Gennaro,*[1] *Stefano Agnoli,*[1]* *and Gaetano Granozzi*[1]

[1] Department of Chemical Sciences, Università degli studi di Padova, Via Marzolo 1, 35131 Padova, Italy

[2] Dipartimento di Scienza dei Materiali, Università di Milano-Bicocca, Via Cozzi 53, 20125 Milano, Italy

*E-mail:, cristiana.divalentin@unimib.it, stefano.agnoli@unipd.it

Keywords: graphene, doped-quantum dots, electrochemical preparation, oxygen reduction reaction

Abstract

Single- and multi- doped graphene quantum dots are synthesized by a simple electrochemical method using water as solvent. The obtained materials are characterized by photoemission spectroscopy and scanning tunneling spectroscopy, in order to get a detailed picture of their chemical and structural properties. The electrochemical activity towards the oxygen reduction reaction of the doped graphene quantum dots is investigated by cyclic voltammetry and rotating disk electrode measurements, observing a clear decrease of the overpotential as a function of the dopant according to the sequence N > B > B,N. Moreover, assisted by density functional calculations of the Gibbs free energy associated to every electron transfer, we demonstrate that the selectivity of the reaction is controlled by the oxidation states of the dopants: oxidized graphene quantum dots follow a two-electron reduction path that leads to the formation of hydrogen peroxide; whereas after the reduction with $NaBH_4$, the same materials favor a four-electron reduction of oxygen to water.

1. Introduction

Graphene (G) is the most fundamental archetype of carbon nanostructures and it has gained a clear standing among materials due to its exceptional properties (superb carrier mobility, good transparency, excellent thermal conductivity etc.). Nowadays, the forefront of research has moved from the study of the basic properties of pure G, to the investigation of chemically modified G (CMG) systems,[1] i.e. doped or functionalized G, and of their composites with other nano-objects, such as nanoparticles or complex molecules. In contrast to the chemical inertness of G, CMGs present a remarkable reactivity, which stems either by defects or by new chemical functionalities. Among CMGs, G oxide (GO) [2] has gained a central role in G technology because it exhibits a tunable electric conductivity,[3] and it can be easily obtained by the oxidation/exfoliation of graphite and processed to obtain wafer scaled devices.[4] Moreover, its solubility in water and facile functionalization makes it the workhorse for wet chemistry applications.[3]

Together with GO, N-doped G is the other main player in the CMG arena. To prepare this material, several preparation methods were developed,[5] e.g. electrochemical reaction with NH_3,[6] exposure to

nitrogen plasma, [7] chemical vapor deposition on metals (Cu and Ni) using a mixture of hydrocarbons, hydrogen and nitrogen containing molecules (NH_3,[8] pyridine,[9] triazine[10]), pyrolysis of polymers[11] solvothermal synthesis[12] or by the chemical reaction between GO and melamine.[13] N-doped G immediately aroused a great deal of attention because, differently from pure G, shows promising activity as a metal-free electrocatalyst in the oxygen reduction reaction (ORR).[5,8,14,]

Recently, other doped G sheets were prepared by different routes: [15,16]

(i) S-doped G by reaction of GO with benzyl disulphide;[17] or by thermal exfoliation in sulfur containing gases[18]

(ii) B-doped G by arc discharge of graphite electrodes in the presence of a H_2 and B_2H_6 mixture,[19] or by annealing GO with B_2O_3 [20] or even other methods;[21,22]

(iii) F-doped G by CF_4 plasma treatment of pure G[23] or by arc discharge of graphite fluoride.[24]

Lately, most advanced synthetic strategies have focused on the introduction of a combination of heteroatoms in G, leading to the preparation of B-N,[25,26,27] S-N,[28,29] and P-N,[14] dually doped materials. These doped G systems exhibit quite interesting properties in terms of electroactivity, in particular in case of the ORR,[16,26,27] but also for alcohol oxidation and hydration reactions.[30,31]

Very recently, amidst CMGs, G quantum dots (GQDs) have emerged as a new class of materials with outstanding properties. They can be considered as small G patches, single or a few-layer-thick and with lateral dimensions below 10 nm. Differently from standard G materials, they are better described as macromolecules and are typically semiconductive with a clear separation between HOMO and LUMO, which is strongly dependent on the geometrical size. Therefore they also exhibit active optical properties like photo- or electro-luminescence, and light up-conversion, opening the door towards applications in photonics, optoelectronics, and photocatalysis.

Moreover, due to their small dimension, GQDs can be easily interfaced to other nano-objects in order to build more complex systems. Similarly to other CMGs, also GQDs can be doped with heteroatoms or functionalized with specific chemical species. This high versatility in the design of complex systems and the easy tunability of their physical properties have generated an immediate interest in the scientific community. GQDs have soon found application as nanolights for bioimaging,[32] sensitizers for photocatalytic systems,[33] and they are envisaged to support a full gamut of practical applications, ranging from road signs and fluorescent clothing to biological markers in medical research.[34]

In a recent paper we have demonstrated that, using a simple electrochemical (EC) procedure starting from GO electrodes, GOQDs solutions can be easily prepared.[35] Here we report a further

development of this method providing a systematic description of the preparation and characterization of single-(B and N) and multi-doped (N and B) GOQDs. We studied their chemical reactivity towards ORR, observing a clear improvement of the catalytic activity in presence of the single dopants, which is further boosted when both B and N are present. Furthermore, DFT calculations were performed in order to rationalize and shed new light on the observed reactivity towards the reduction of oxygen. We found that the ORR selectivity in GOQDs can be switched quite easily from a $2e^-$ electron path to a $4e^-$ electron path simply by chemically reducing the doped-materials. The presence of oxygen functional groups therefore represents a pivotal factor for controlling the chemical selectivity, which so far has been completely overlooked. This work therefore provides a basic understanding for a rational design of ORR electrocatalysts operating at very small overpotential that can either selectively reduce oxygen to water, or when oxidized, can efficiently produce hydrogen peroxide.

2. Experimental Section

Only basic information is reported in the present section. See supplementary information (SI) for more details.

The preparation of GO microflakes was performed using the modified Hummer's oxidation reaction.[36,37] The characterization of the starting GO material was carried out by UV-VIS and X-ray Photoelectron (XPS) Spectroscopies. The lateral dimensions of the GO sheets, were determined by Scanning Electron Microscopy (SEM) measurements depositing the GO sheets by means of Anodic Electrophoretic Deposition on P:Si (100) wafers. The lateral distribution of the GO microflakes is characterized by a large distribution, with sizes between 1 and 5 μm.

The EC preparation of GOQDs[35,38,39] was carried out at 25°C in a standard three-electrode EC cell, using a Pt ring as Counter Electrode (CE) and a saturated $Ag/AgCl/Cl^-$ electrode as Reference Electrode (RE), cycling the potential between ±3.0 V at a scan rate of 500 mV/s.

The Working Electrodes (WE) were built from a Glassy Carbon (GC) plate. The EC synthesis of doped-GOQDs were carried out adding to a 0.1 M Phosphate Buffer Solution (PBS) the molecular precursor chosen as dopant source.

The pure and doped-GOQDs were then collected after about 2000 potential cycles. **Table 1** reports the experimental conditions for the different syntheses.

Table 1. Experimental conditions for the synthesis of doped-GOQDs.

	Electrolyte	Dopant Molecule [1]	Final pH [2]	
GOQDs	PBS 0.1M (pH 6.86)	-	6.86	A
B-GOQDs	PBS 0.1M (pH 11.20)[3]	1,4-phenylenebis(boronic acid) (**1**) (100 mM)	11.20	B
N-GOQDs	PBS 0.1M (pH 6.86) PBS 0.1M (pH 1.85)[4]	*a.* ethylenediamine (**2**) (100 mM) *b.* 1,10-phenantroline (**3**) (100 mM)	11.30 1.85	C D
B,N-GOQDs	PBS 0.1M (pH 6.86)	ethylenediamine (100 mM) + 1,4-phenylenebis(boronic acid) (100 mM)	11.30	E

[1] See Figure 1. The quantity of the dopant added was determined in order to obtain a final dopant volumetric concentration of 100 mM.
[2] The pH was measured after the addition of the dopant molecule to the 0.1 M buffer solution.
[3] The pH was increased by adding a few drops of a 10 M NaOH solution, in order to solubilize the doping molecules.
[4] The pH was decreased by adding a few drops of concentrated H_3PO_4 (85 %), in order to solubilize the 1,10-phenantroline (by protonation of the pyridinic nitrogens).

More details on the procedures and methods are reported in the SI. Thin films of GOQDs drop cast on polycrystalline copper foils were used for the SEM and XPS characterizations. Technical details are provided in the SI.

The electrochemical activity measurements towards the ORR were carried out by cycling voltammetry (CV) and rotating disk electrode (RDE). A conventional three-electrode configuration consisting of a Pt wire as CE and a saturated $Ag/AgCl/Cl^-_{(sat.)}$ as RE was used (standard electrode potential $E^{\Theta}_{Ag/AgCl\ (sat.)} = 0.197$ V with respect to the standard hydrogen electrode, SHE). All the experimental potentials reported in this work are referred to this RE.

In order to prepare the catalyst ink, 4 mg of pure or doped-GOQDs were dissolved in 1 mL of bi-distilled water; after the addition of perfluorinated Nafion alcoholic solution (5%, Aldrich), and the obtained solution was ultra-sonicated for 30 minutes. Then, the WE was prepared by depositing 15 mL of the ink onto a polished GC disk mounted on a RDE tip (Autolab RDE-2), which exposed an area of 0.071 cm^2 to the electrolyte. Finally, the drop-casted film was dried in air at room temperature (RT) for about 12 h.

All the calculations were performed with the GAUSSIAN09[40] (G09) package and the B3LYP[41,42] functional. Spin polarization was taken into account in the case of open shell systems. The model for pure G QDs is a circumcoronene molecule ($C_{54}H_{18}$). The orbitals were described with Gaussian basis functions 6-311+G* for the inner five C atoms, the B and N atoms, and the O and H atoms involved in the water formation; 6-31G* for the rest of the model. All atoms were allowed to relax during the geometry optimization without any symmetry constraint.

Vibrational frequencies in the harmonic approximation were calculated for all optimized structures and used, unscaled, to compute zero point energies, enthalpies and Gibbs free energies.

The conventional theoretical reference electrode is the standard hydrogen electrode, SHE. [43] At pH = 0 and at potential $U = 0$ V vs SHE, the reaction $H^+ + e^- \leftrightarrow ½\ H_2$ is in equilibrium at 1 bar $H_{2(g)}$ at 298 K, thus G ($H^+ + e^-$) = G ($½H_2$). The free-energy difference of the full ORR with the present setup is -4.64 eV, which we consider in more than satisfactory agreement with the experimental value of -4.92 eV. The free energy of OH^- is derived as G (OH^-) = G ($H_2O_{(l)}$) - G (H^+), where G (H^+) is corrected by - kT × ln 10 × pH, to account for the pH conditions. However, for a direct comparison with experiments, the potential U values discussed later in the text (Section 3.4) are referred to the saturated $Ag/AgCl/Cl^-_{(sat.)}$ reference electrode.

The contribution of bulk solvent (water) effects to the Gibbs free energy (G_{sol}) was computed using the polarizable continuum model (PCM) in the SMD version [44,45] implemented in the Gaussian09 package.

3. Results and Discussion

3.1 Preparation

The electrochemical etching of an electrode constituted by G or GO can produce a solution of highly luminescent G or GOQDs.[38,52] A suitable change of the experimental conditions (i.e. solvent, supporting electrolyte etc.) allows the preparation of doped-G or GOQDs.[46,50] In particular, the use of an aqueous environment for the synthesis of GOQDs is more economic, environmental friendly and poses fewer problems regarding the purification of the final product.[47] To our best knowledge, only the present study (along with the recent work on B-doped G quantum dots (GQDs) by Fan et al.[48]) reports the electrochemical synthesis of doped and co-doped GOQDs by adding a molecular dopant precursor to an aqueous electrolytic medium. For the synthesis of doped-GOQDs (as described in Table 1 and SI), a dopant molecule (e.g. 1,4-phenylenebis(boronic acid), ethylendiamine, 1,10-phenanthroline) was added to the electrolytic solution to provide the doping heteroatoms. Similarly, to prepare co-doped-systems as B,N-GOQDs a mixture of dopant molecules was introduced in the electrochemical cell.

The formation of GOQDs involves the oxidation of the C-C bonds and the intercalation of the electrolyte ions into the structure of the GO electrode, with the consequent release in solution of the GOQDs.[35,47,49] The absence of distinct voltammetric peaks in the polarization curves shown in Figure S1, suggests that the formation mechanism of doped-GOQDs can be modeled as sketched in Figure 1.

In the first step (1), a dopant molecule/WE bond is formed via a radical mediated process: since the synthesis occurs under drastic conditions (i.e., at high applied potential beyond the stability window of the solvent), a huge amount of highly reactive radicals is formed, either on the WE surface, or transferred to the dopant molecule. This implies also a possible rupture of the intramolecular bonds in the dopant molecule (step 2), with the formation of several types of functional groups, as evidenced by XPS measurements (see section 3.2). During step (3), the formation of linear chains of epoxy groups and carbonyl pairs[50,51,52] determines the unzipping of GO nano-fragments and the consequent release in solution of doped-GOQDs decorated at the edges by oxygen groups (step-4).[35,52]

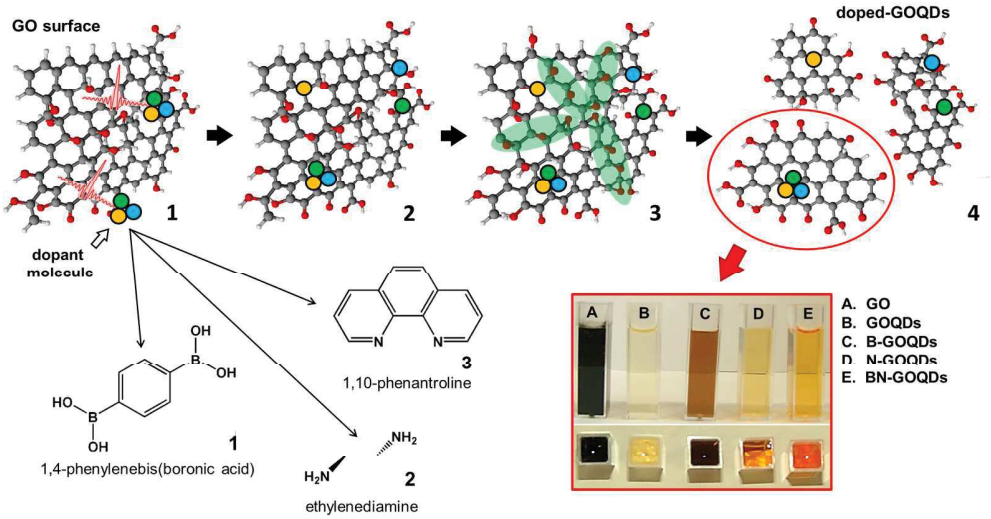

Figure 1. Pictorial model of the doping mechanism occurring during the synthesis of doped-GOQDs, reporting the molecular structures of the dopant molecules used in this work (**1**: 1,4-phenylenebis(boronic acid), **2**: ethylenediamine, **3**: 1,10-phenantroline) and a digital picture, under environmental light, of the different doped and co-doped-GOQDs solutions produced via EC etching of a GO WE.

3.2 Chemical and structural characterization.

XPS measurements were performed to determine the chemical composition of the doped-GOQDs. The XPS survey spectra reported in Figure S2 show a predominant graphitic C 1s photoemission line at a binding energy (BE) of 284.6 eV and an O 1s photoemission peak centered at 531.6 eV. The C/O atomic ratio is almost equivalent, with slight differences, for all doped-GOQDs, and it is equal to 4.3. The pure GOQDs show a slightly lower C/O atomic ratio, which is equal to 3.8. Figure S2 shows the presence of B and N 1s photoemission lines in the survey spectra of B- and N-doped GOQDs (hereafter B- and N-GOQDs), respectively. On the other hand, both B and N 1s peaks are visible in the survey spectrum of B,N-co-doped GOQDs (hereafter B,N-GOQDs). These findings confirm the successful introduction of heteroatoms into the GOQDs by electrochemical etching of the GO WE in

the dopant-containing electrolyte. Table 2 reports the elemental compositions (at%) for all the prepared systems, which are similar in terms of dopant concentration to those already reported in literature for analogous materials.[53,54]

In order to have a better understanding of the different chemical species introduced by the doping, the photoemission spectra of carbon and dopants were separated into single chemically shifted components, as reported in Figure 2.

Table 2. Elemental composition (calculated from XPS quantitative analysis) for the doped and co-doped-systems studied in this work.

	B (at%)	**N** (at%)
B-GOQDs	5.3	-
N-GOQDs	-	5.1
B,N-GOQDs	5.2	4.7

The multipeak analysis of the C 1s photoemission line of pure GOQDs (Figure 2.a) indicates the presence of a graphitic sp^2 core (284.6 eV), whose edges are decorated by several oxygen functional groups, such as C–O (286.4 eV), C=O (288.1 eV) and O–C=O (289.2 eV).[52,55]

In the case of B-GOQDs, the B 1s fit reveals (see Figure 2.b) the presence of three different B-based chemical defects. The first component (**1**), centered at 189.6 eV, is related to B substituting C in the sp^2 network.[19, 48] This component has its direct counterpart in the C 1s fit reported in Figure 2.a (the component associated with B–Csp^2 bonds is localized at 283.5 eV.[19,26,48,73] The other two B 1s components are related to B–O bonds (Figure 2.b), namely G–BO (**2**, 190.6 eV) and to G–BO_2 (**3**, 192.0 eV).[19,48,73,74] The presence of these oxidized groups is connected to the interaction between the dopant molecule (or, as discussed above, its unstable molecular fragments) and the oxygen functional groups that decorate the GO surface[30] or that are introduced by the oxidation of water during the anodic sweep up to +3.0 V.[35] The present method allows introducing a high percentage of substitutional B atoms in the graphitic core of the GOQDs, (whose component counts for 27 % of the total B 1s photoemission area). As regards the N-GOQDs, from the comparison between the C 1s spectrum of pure and N-GOQDs (Figure 2.a), a component connected to C-N groups can be identified at 285.8 eV.[39, 56] The multicomponent fit of the N 1s photoemission line, reported in Figure 2.c, shows four different chemical components centered at a BE of 398.6 eV, 399.9 eV, 401.1 eV and 402.4 eV, which correspond to pyridinic (**1**), pyrrolic (**2**), graphitic (**3**) and pyridine oxide groups (**4**), respectively.[57,58,59,60]

The main component of the N 1s photoemission line in the case of the synthesis with ethylendiammine (in parenthesis data for 1,10- phenantroline) is constituted by the pyrrolic N group (**2**), which counts for 41 % (48%) of the total N 1s photoemission area; for both doping sources, pyridinic (**1**) and graphitic N (**3**) species are equivalently present in the N 1s spectrum, counting for 25 % (24%) and 27 % (20%), respectively. Only 10 % (5%) of the total N is present as oxidized species, in which N is directly bonded to an O atom (**4**).

Interestingly, the use of a primary alkyl ammine (ethylendiammine) or of an aromatic π–conjugated ammine (1,10-phenantroline) does not strongly influence the chemical state of nitrogen atoms transferred to the GOQDs.

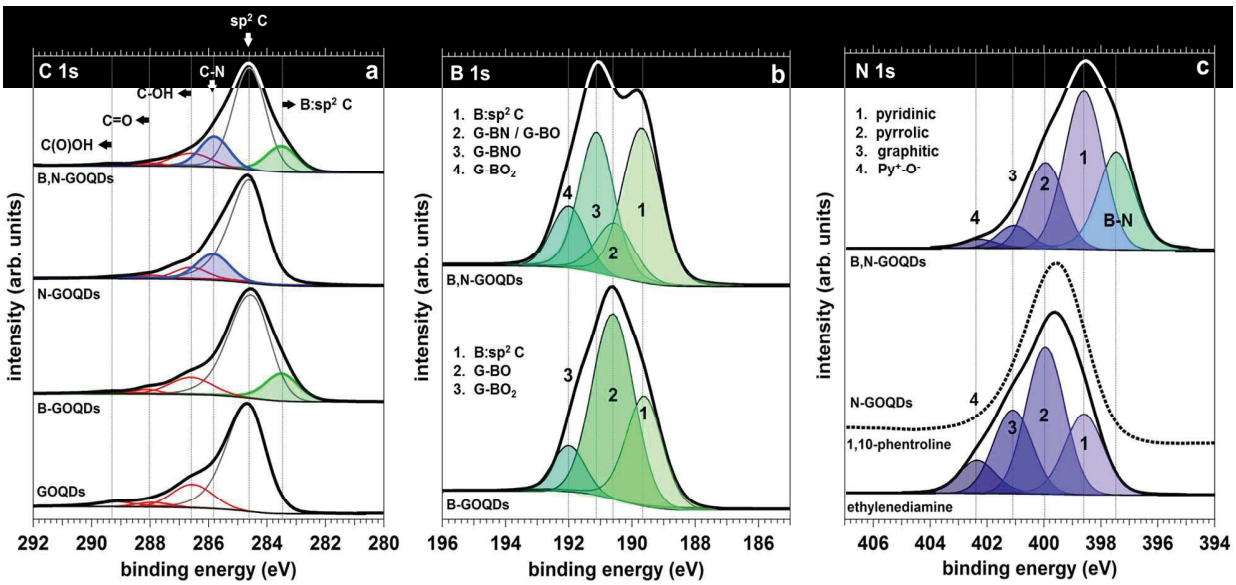

Figure 2. a: Multicomponent fits of the C 1s XPS peaks for pure, B-, N- and B,N-GOQDs. Figures b and c report the relative dopant photoemission line fits, for B 1s and N 1s, respectively.

This result is in agreement with the mechanism proposed for the preparation of doped-GOQDs, which is mainly mediated by highly reactive radicals. This implies that the obtained doped-GOQDs do not keep "chemical memory" of the particular structure of the parent dopant, and the number and the type of the functional groups introduced during the EC synthesis in the GOQDs depend only on the formation kinetics of the dopant radicals.

Since synergetic effects between different heteroatoms present in the graphitic networks can promote an enhanced catalytic activity in several electrochemical reactions (and, in particular, in the ORR),[26,28,53,61] we employed a combination of ethylendiammine/phenyl diboronic acid in order to prepare B,N-GOQDs. The C 1s multicomponent fit (reported in Figure 2.a) shows the presence of both C–N and B–sp^2C bonds (whose components are centered at 285.7 eV and 283.6 eV,

respectively). Similarly, the B 1s photoemission spectrum reported in Figure 2.b, shows the presence of the B–sp^2C bond component (**1**) centered at 189.6 eV.[19,26,48,73] The B,N co-doping affects the relative amount of the B-sp^2C bond, which changes from 27% in the case of B–GOQDs to about 38% in the case of B,N-GOQDs. As regard to the second component, centered at 190.6 eV (**2**), the small difference in the electronegativity between N and O (0.4) does not allow discriminating between the G–BO and the G–BN groups. Then, this component has to be identified as the envelope of the two single G–BO and G–BN components. This observation will be further supported by the photoemission data in the section 3.3.2. The new peak, centered at 191.1 eV (**3**), is assigned to G–BNO groups, that is boron atoms bonded to both nitrogen and oxygen.[74] This observation is also highlighted by the difference spectra reported in Figure S3, for the B and N 1s photoemission peaks. This directly proves that the co-doping is not the simple sum of the two heteroatoms, but involves a direct interaction between the two distinct dopants.[53,61] Figure 2.b and Figure S3 show that the intensity of the B 1s photoemission peak in the case of the B,N-GOQDs is stronger at high BE with respect to the B-doped system. Similarly, an opposite phenomenon is observed in the N 1s photoemission peak, in which a clear shift towards low BEs takes place as a result of the B–N bond formation. This can be explained by the large difference in the electronegativity of B and N (i.e. 1.0), which implies that the generation of direct B–N bonds causes an upshift of the B 1s peak (Figure S3a) and the concomitant downshift of the N 1s peak (Figure S3b), with respect to the signals of the single doped systems.

The chemical state of N in B,N-GOQDs is elucidated by the identification of the chemically shifted components in the photoemission spectrum, as reported in Figure 2.c. The formation of C–BN groups, observed in the B 1s data, is confirmed by the presence of a highly intense C–BN component in the N 1s spectrum, centered at 397.5 eV,[61,62] which represents the 31 % of the whole peak area. By making reference to the above reported discussion on N-GOQDs, we can also identify other four different chemically-shifted components centered at 398.6 eV, 400.0 eV, 401.1 eV and 402.4 eV, which correspond to pyridinic (**1**), pyrrolic (**2**), graphitic (**3**) and pyridine oxide groups (**4**), respectively. It is noteworthy that the B,N co-doping seems to trigger a higher selectivity for the formation of pyridinic groups (**1**) in the B,N-GOQDs, as compared to the N-GOQDs. In fact, the pyridinic component passes from 25% (in the case of N-GOQDs) to 39% (in the case of B,N-GOQDs). This could have important consequences in the catalytic properties of this material, since the carbon atoms close to pyridinic groups are considered to be the active sites for the ORR,[63] especially in alkaline conditions.[53,64] At the same time, we observe a depletion of the content of pyrrolic groups (**2**), (which passes from 41 % in the case of N-GOQDs to 19 % in the case of B,N-GOQDs) and in the content of

N-graphitic defects (**3**) (reduced from a value of 24 % in the case of N-GOQDs to 9 % in the case of B,N-GOQDs). Finally, the B,N co-doping can reduce efficiently the amount of oxidized N groups (**4**), which decrease from 10 % to 2 % of the total peak area, with respect to the single doped N-GOQDs.

STM measurements on diluted drop casted solutions of GOQDs provide direct evidence of the presence of nano-fragmented GO. After the evaporation of the solvent, GOQDs can be adsorbed in a flatly lying geometry on a HOPG substrate due to π-π interactions. [65] As experimentally observed, the surface diffusion of single GOQD units is relatively easy at RT, probably because the irregular structure of the GOQD edges weakens an effective interaction with the substrate. For this reason, mild tunneling conditions were used to limit unwanted tip induced diffusion. Generally, no lateral order is detected and single randomly scattered GOQDs are found. High-resolution topographies (Figure 3) indicate that the pure GOQDs display a quasi-circular shapes (Figure 3.a), whereas the B- and N-GOQDs (Figure 3.b,c) show straight edges resembling triangular shapes. Straight and round mixed edges instead are visible on B,N-GOQDs (Figure 3.d). These features are attributed to the exposure of specific graphitic crystal faces[66,67] as a consequence of the unzipping reactions that originated the nano-fragments. All the observed pure, doped and co-doped -GOQDs fall into a 1 nm sharp size dispersion centered at 2 nm, with heights in the 0.4-0.6 nm range, confirming that the prepared GOQDs are single-layer-thick.[68] The STM contrast is substantially unaffected by variations of sign or magnitude of the applied voltage. No atomic resolution could be achieved on the GOQDs, due to the irregularities and functionalization of the edges. The close proximity of the edges, moreover, causes the electron wave functions to be scattered,[66,69] interfering with the electronic states of edge defects or with the electronic states of the dopant atoms. This phenomenon may be the reason of the experimental observation of the invariance of the STM contrast with respect to the applied voltage.

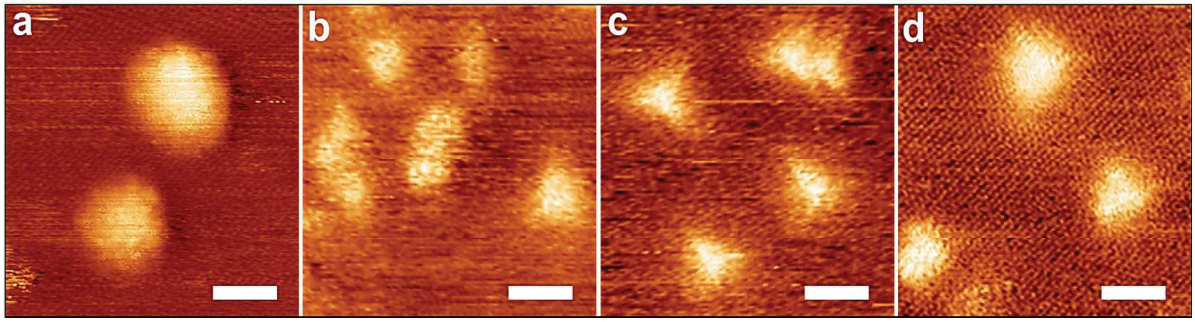

Figure 3. STM topographies of non-doped (a) and doped (b-d) GOQDs at the HOPG/air interface. All images are 10 × 10 nm^2 size, obtained with horizontal fast line scanning. The scale bar is 2 nm. a: GOQDs (E = 0.08 V, I = 100 pA); b: B-GOQDs (E = 0.15 V, I = 150 pA); c: N-GOQDs (E = 0.15 V, I = 100 pA); d: B,N-GOQDs (E = 0.10 V, I = 250 pA).

3.3 Oxygen reduction reaction catalytic activity of pure and doped-GOQDs

Apart from their unique photophysical properties, (which will be addressed in another work[Error! Bookmark not defined.]), doped-GOQDs are also expected to possess electrocatalytic activity towards the ORR, as widely reported in literature. In particular, B-[53,88], N-[46,58,59,70,71,88], S-doped[17,53,72,88] and B,N-codoped[14,25,26,27,73,74,75] G-based materials have shown high activities towards the reduction of oxygen, but these studies have been focused on 3D materials.[39,46,70,76] According to our best knowledge, only the work of Li et al.[77] reports the study of the catalytic properties of genuine GQDs *per se*, considered as distinct molecular units. Therefore, a study of the catalytic performances of the pure and doped-GOQDs is still missing in literature.

The reduction of oxygen catalyzed by graphitic and G based-materials in alkaline electrolytes follows the reaction mechanism proposed by Strelko et al., [78, 79, 88] reported schematically in Figure 4.

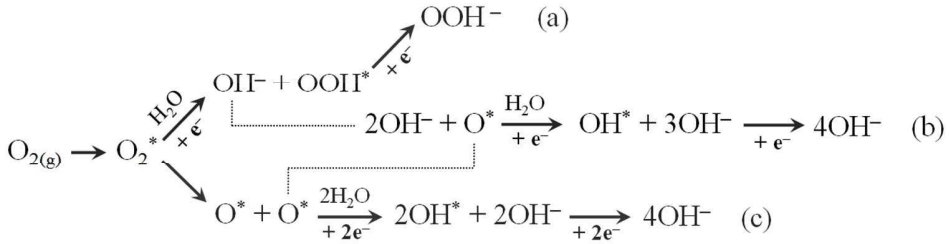

Figure 4. ORR possible pathways in alkaline medium; a mechanism depicts the $2e^-$ pathway, while b and c are $4e^-$ reactions. The * symbol is used for the adsorbed species.

As well known in literature,[64,79,88] ORR can occur, accordingly to the scheme reported in Figure 4, either by a two-electron reaction ($2e^-$, Figure 4.a), with the formation of OOH^- intermediate, or by a more efficient direct four-electron mechanism ($4e^-$, Figure 4.b and c).

Since the rate determining step is represented by the desorption rate of OOH* or OH* species (which characterizes the selectivity of the catalytic material towards the $2e^-$ or $4e^-$ pathway, respectively),[79] it is clear that the increase in the kinetics of this electronic transfer plays a fundamental role in the catalytic performances towards the ORR.

To investigate the catalytic properties of our doped-GOQDs, films of hundred nanometers were drop-casted from concentrated aqueous solutions onto clean glassy carbon (GC), using Nafion[80] as binder polymer to enhance both the mechanical stability and proton and OH^- permeability of the material.[80] SEM micrographs of the prepared films are reported in Figure S4.

Following this procedure, it was possible to investigate the real electrochemical response of the doped-GOQDs without performing any further preparation, differently to what is currently reported

in literature,[39,46] which may change the chemical nature or the molecular structure of the quantum dots themselves.

Figure 5 reports the polarization curves for the O_2 reduction on pure- (a), B- (b), N- (c), B,N-GOQDs (d), acquired in O_2-saturated KOH 0.1 M solution. Every system shows a well-defined cathodic feature for the irreversible reduction of O_2. As reported in Table 3, the doped systems display a positive shift of the onset potential with respect to pure GOQDs, indicating that the introduction of the heteroatoms promotes the catalytic activity for ORR as already reported in the literature.[39,46,53,57,59,70]

In the case of boron doping, the presence of substitutional atoms has a dual effect: on the one hand, since the electronegativity in boron is lower than in carbon, the positively polarized boron atoms in the graphitic lattice attract the nucleophilic oxygen molecules leading to efficient chemisorption; on the other hand, boron sites can also act as electron shuttles for the electron density of the graphitic π electron system going through the p_z orbital of boron to the chemisorbed O_2 molecule. [81,82] Regarding the N-GOQDs, although it is well-established that the introduction of N doping can boost the ORR catalytic activity of carbon-based materials,[39,46,58,60,70,71,77,83,88] the identity and the exact role of the electrocatalytically active centers are still under debate. Recent works by Lai et al.[59] and Xing et al. [63] suggest that the carbon atom next to a pyridinic nitrogen is involved in the reaction with oxygen favoring its adsorption and further reaction. More generally, it is commonly accepted[59,84,85] that N-based defects in G increase the density of π states near the Fermi level with the consequent reduction of the work function. The relative high electron withdrawing power of N atoms reduces the electron density on the adjacent C nuclei, with a net charge transfer from C to N. Furthermore, N atoms can back-donate electrons to the adjacent C p_z orbitals involved in the π-conjugated system. The donation and back-donation processes facilitate the O_2 adsorption on the C atoms nearest neighbor to the N atom, and then the subsequent dissociation accordingly to the scheme reported in Figure 4. This determines a faster kinetic in the reduction of oxygen and then a lower overpotential needed for the reaction. To conclude, the loss of the electroneutrality of graphitic materials to create charged sites favorable for O_2 adsorption seems to be a key factor for enhancing ORR activity,[86] regardless of whether the dopants are B or N atoms.[59,60,88]

Concerning the co-doped GOQDs, they are characterized by the highest activity for the reduction of oxygen (i.e. lowest overpotential), compared to the performances shown by the other materials.[26,61]

The origin of this behavior is quite difficult to trace, however the photoemission data clearly indicate that the presence of nitrogen determines a shift towards higher BE in the centroid of the photoemission peak of boron, which indicates an average higher positive charge on boron sites,

which therefore can be more efficient in the adsorption of oxygen. Moreover, in B,N-GOQDs materials there is an increase in the pyridinic component, apparently stabilized by the presence of boron, supporting the idea that these sites are indeed the most active players involved in the ORR.

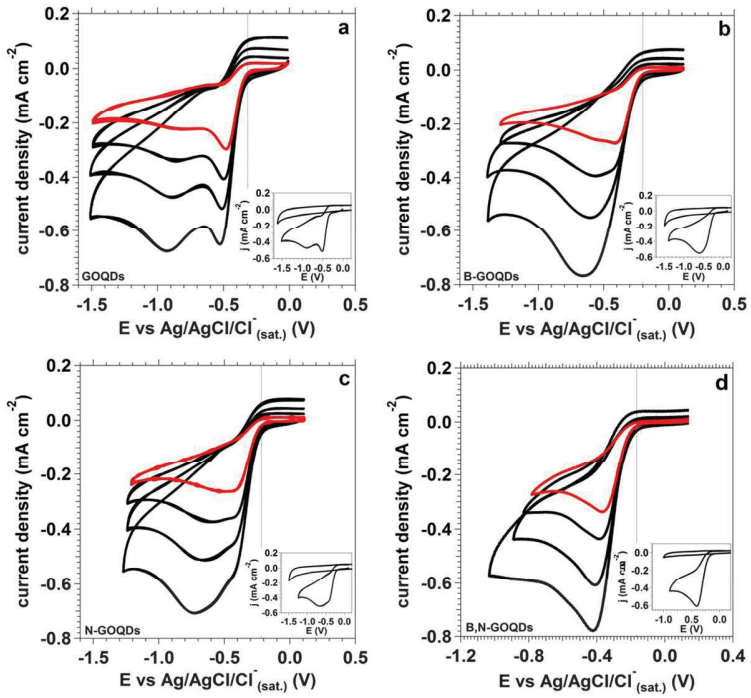

Figure 5. CVs of pure- (a), B- (b), N- (c) and B,N-GOQDs (d) in O_2-saturated 0.1 M KOH solution, at different potential scan rate (10, 20, 50 and 100 mV/s). For every each system, the inset report the CVs (at 50 mV/s) acquired in Ar- and in O_2-saturated 0.1 M KOH solutions.

3.3.1 ORR mechanism for pure and doped-GOQDs

In order to obtain the number of the exchanged electrons and, in this way, to clarify the mechanism of the reduction of oxygen on the doped-GOQDs, we carried out rotating disk electrode (RDE) measurements.

Linear Sweep Voltammetry (LSV) curves of the ORR on the studied systems are reported in Figure 6 for different electrode rotation speeds. The measured current densities show a typical uprising as the electrode rotation rate increases, due to the enhanced diffusion of electrolytes.[87,88] The transferred electron number per O_2 molecule involved in the ORR process and, therefore, the predominant reaction pathway, was determined using the Koutecky-Levich formalism (details are provided in the SI). The parallel and straight fitting lines, reported in Figure 6 for each system and for different potential values across the LSV, imply a first-order reaction with respect to dissolved oxygen.[88]

Interestingly, the *n* values for pure-, B-, N- and B,N-GOQDs are close to 2, as reported in Table 3, with just minor changes as a function of the potential. Apparently, the production of peroxidic intermediates (as described by the $2e^-$ mechanism reported in Figure 4) is in contradiction with the commonly accepted $4e^-$ pathway for the reduction of oxygen on doped-G and GOQDs.[15,46,53,59,60,70] However, in the cited literature papers, the G-based QDs were employed merely as a "dopant source" for 3D-structured materials.[39,46] On the other hand, the size of the sp^2 lattice influences the ORR behavior.[88] It has been reported in fact that the reduction in the lateral size of N-doped G, up to the nanometer scale, leads to a significant enhancement in the hydrogen peroxide production, even in alkaline electrolytes.[77] Thence, our results are in line with these previous data, showing that the introduction of dopant atoms (N or B) positively enhances the catalytic activity of the GOQDs. The high selectivity of pure or doped-GOQDs towards the bi-electronic reaction path suggests their application as nanocatalysts for the selective production of H_2O_2 to be used in water remediation or organic microflow synthesis.

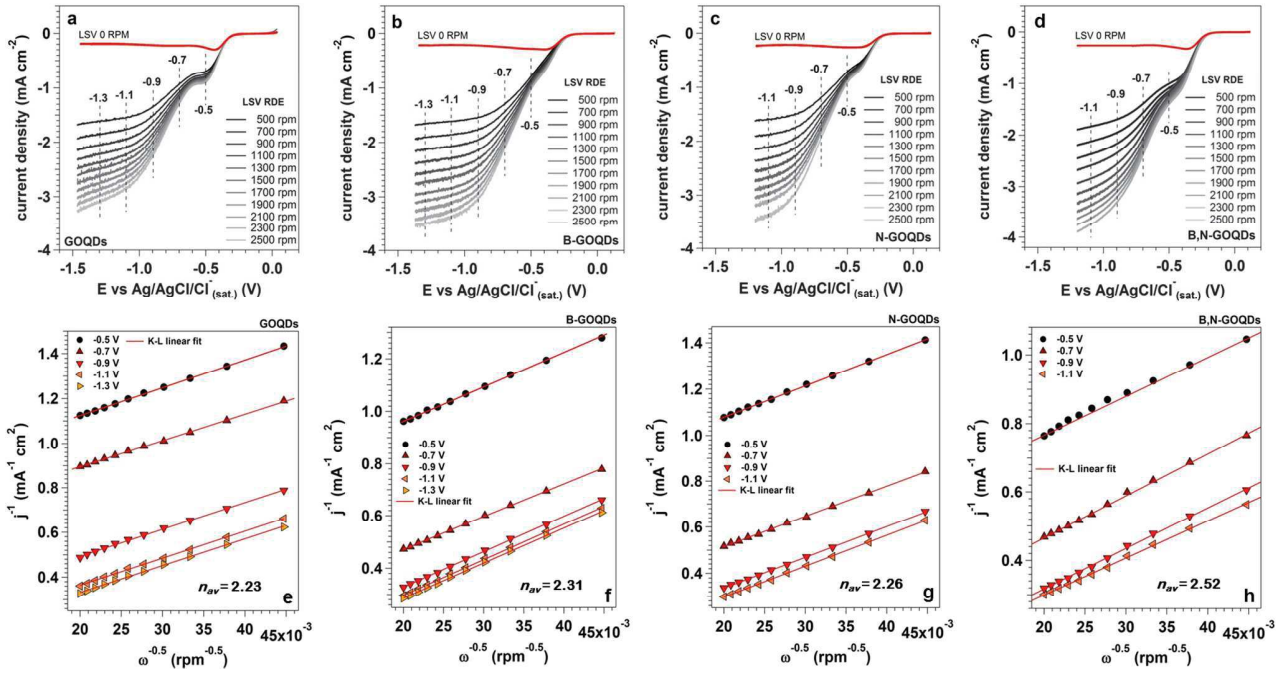

Figure 6. RDE linear sweeps for pure- (a), B- (b), N- (c) and B,N- (d) GOQDs acquired in O_2-saturated 0.1 M KOH solution, for different rotation speeds. Koutecky-Levich plots for different potential derived from the RDE measurements, for pure- (e), B- (f), N- (g) and B,N-GOQDs (h), respectively. The average numbers of the exchanged electrons (n_{av}) reported in the figures have been obtained as average number of the values reported in Table 3.

3.3.2 The role of the oxygen functional groups in the ORR mechanism. Chemical reduction of doped-GOQDs

In order to point out the role played by the oxygen functional groups, decorating the edges of the doped-GOQDs, on the activity and selectivity towards the ORR, we have performed a mild chemical reduction with $NaBH_4$ (for 12 h at RT, see SI for details). Figure 7 reports the multipeak analysis of C 1s and of the dopant core levels photoemission lines for B- and N-GOQDs after the chemical reduction (hereafter red-B-GOQDs and red-N-GOQDs, respectively).

In both cases, the chemical reduction treatment determines an important decrease of the oxidized species, such as G–BO_2 and N–O groups present in the B- and N-GOQDs, respectively. Thus, after the chemical reduction the doped-GOQDs are characterized by a C sp^2 core with the presence of several dopant species (as discussed above), but with a very limited oxygen content: the C/O ratio passes from 4.3 for the as-prepared systems to about 10.6 in the case of the chemically reduced B-, N- and B,N-GOQDs.

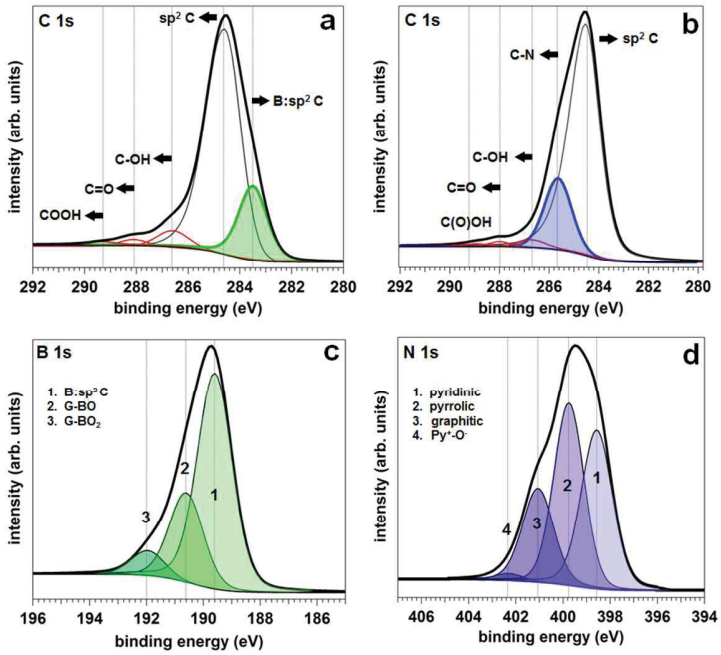

Figure 7. XPS analysis and relative fits of the C 1s (a, b) and B and N 1s (c,d) photoemission peaks for the red-B- and red-N-GOQDs, respectively.

As shown by Figure 8, the removal of the oxygen functional groups on both systems goes together with an increase in the activity with respect to the as-prepared systems. In particular, in the case of B-GOQDs, the onset potential increases from –0.194 V to –0.169 after the chemical reduction. Similarly, the peak potential undergoes a shift towards less cathodic potential, with a net overpotential gain of 90 mV after the $NaBH_4$ treatment (see Table 3).

The beneficial effect of the chemical reduction on the reactivity is also observed in the case of N-doping. Figure 8 shows an oxygen reduction peak centered at –0.354 V in the case of red-N-GOQDs, which is upward shifted by 89 mV with respect to the value observed on pristine N-GOQDs. Then, we can conclude that the removal of oxygen functional groups from the doped-GOQDs represents a facile way to boost the catalytic activity of these systems: both B- and N-GOQDs exhibit an overpotential decrease of about 90 mV after the chemical reduction with $NaBH_4$.

Interestingly, the presence of oxygen groups not only influences the activity, but also the selectivity of these materials towards the two different paths followed by the ORR. Figures 8.c and f show that the number of exchanged electrons after the chemical reduction of B- and N-GOQDs is close to 4 for both systems. Since *n* was close to 2 for the as-prepared doped-GOQDs, this states that type of mechanism and therefore the selectivity of the ORR is driven by the presence or absence of the oxygen functional groups that decorate the doped-GOQDs.

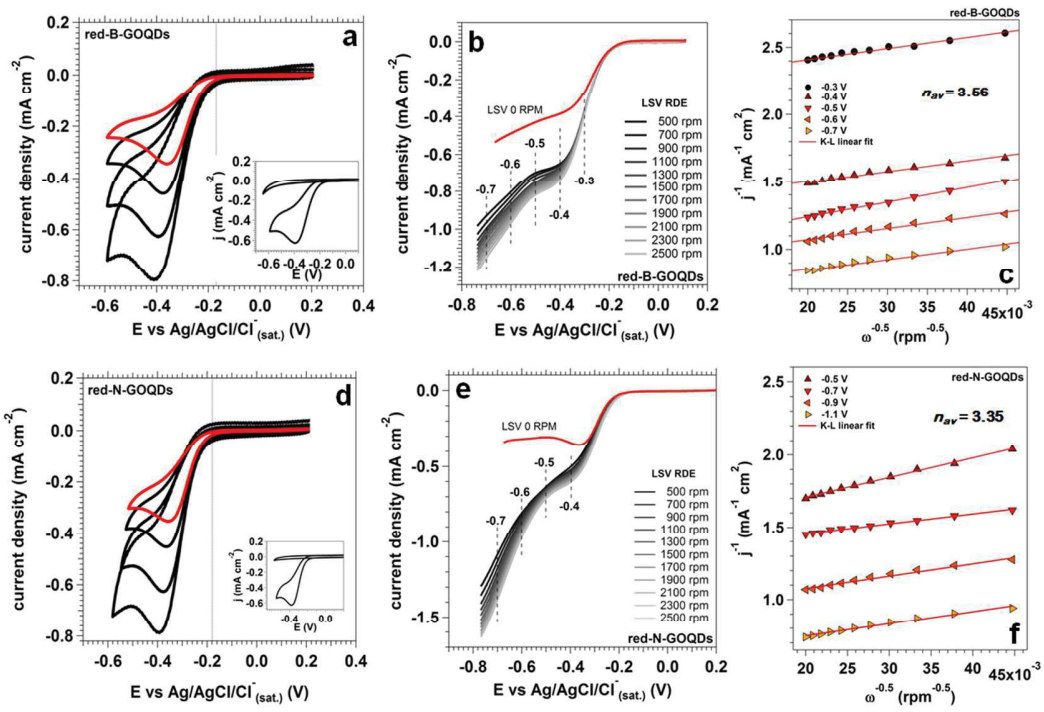

Figure 8. Catalytic tests for red-B- (a, b, c) and red-N-GOQDs (d, e, f); a, d: CVs in O_2-saturated 0.1 M KOH solution, at different potential scan rate (10, 20, 50 and 100 mV/s). The reported insets show the CVs (at 50 mV/s) acquired in Ar- and in O_2-saturated 0.1 M KOH solutions; b, e: RDE linear sweeps acquired in O_2-saturated 0.1 M KOH solution; c, f: Koutecky-Levich plots for different potential derived from the RDE measurements. The average numbers of the exchanged electrons (n_{av}) reported in the figures have been obtained as average number of the values reported in Table 3.

This will be further discussed in the next section where a theoretical modeling by DFT calculations is presented. In the light of these findings, we have investigated the reduction effect with $NaBH_4$ on the dual doped GOQDs, which are the most active and promising materials,[15,53,88] a similar $4e^-$ mechanism by eliminating the oxygen species by reduction with $NaBH_4$. Figure 9.a, b and c report the B, C and N 1s photoemission lines separated into chemically shifted components, for the B,N-GOQDs after the reduction procedure (hereafter red-B,N-GOQDs). The reduction treatment leaves substantially unchanged the chemical nature of the B,N-GOQDs, with the only exception of the oxidized components, which show a drastic decrease as consequence of the reduction treatment.

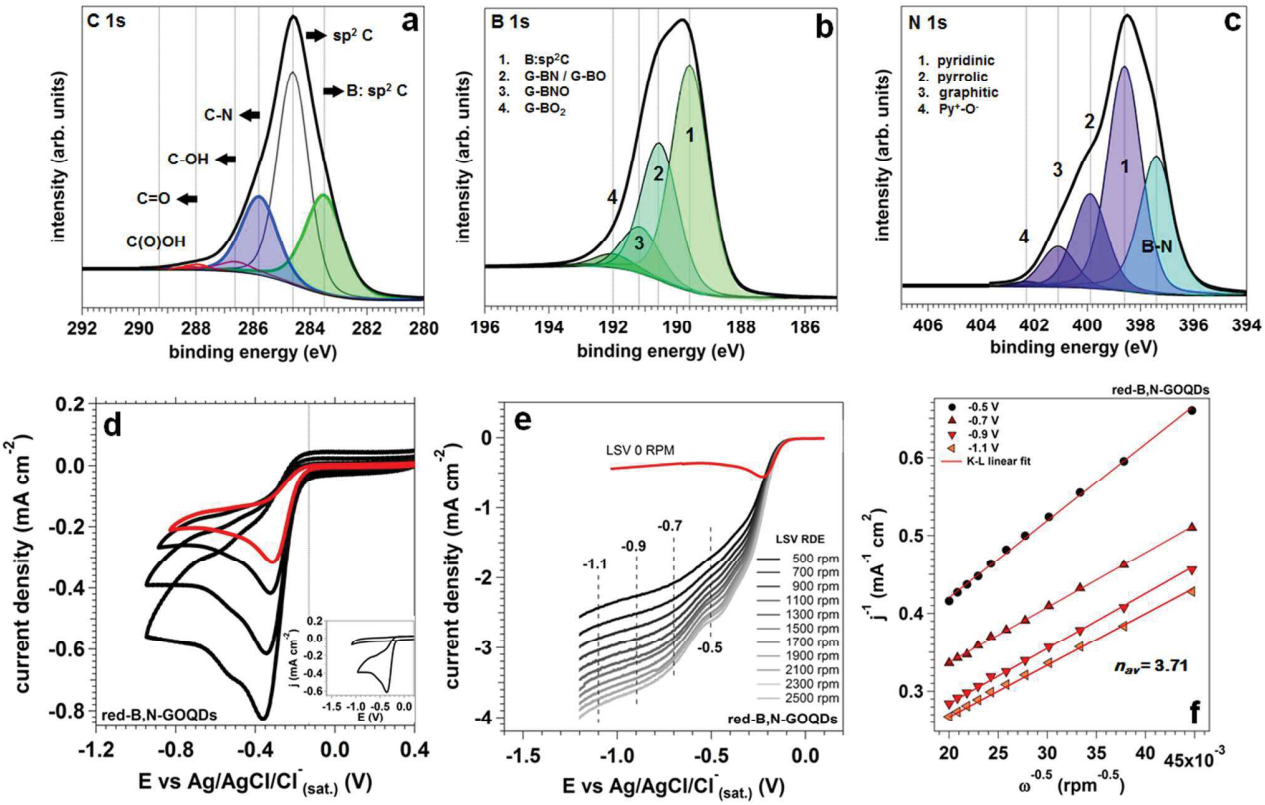

Figure 9. XPS analysis and catalytic tests for red-B,N-GOQDs; a, b, c: multicomponent fits on B, C and N 1s photoemission lines; d: CVs in O_2-saturated 0.1 M KOH solution, at different potential scan rate (10, 20, 50 and 100 mV/s). The inset report the CVs (at 50 mV/s) acquired in Ar- and in O_2-saturated 0.1 M KOH solutions; e: RDE linear sweeps acquired in O_2-saturated 0.1 M KOH solution; f: Koutecky-Levich plots for different potential derived from the RDE measurements. The average numbers of the exchanged electrons (n_{av}) reported in the figures have been obtained as average number of the values reported in Table 3.

Interestingly, the component labeled as **2** in Figure 9.b exhibits an important intensity increase after the chemical reduction treatment, whereas the oxidized G–BNO component (**3**) decreases. This can be explained assuming that the G–BN groups are generated by the reduction of their relative oxidized

precursor (that is the G–BNO species) and admitting that their BE is centered at 190.6 eV (overlapping in this way with the G–BO component, as already mentioned above in the section 3.2). It is very important to note that the fully oxidized G-BO_2 component (**4**) practically disappears after the $NaBH_4$ treatment. The relative overall decrease of the oxidized species clearly improves the catalytic activity of the material. This will be further discussed in the next section of the theoretical modeling.

As shown in Figure 9.c, the onset of the oxygen reduction peak is at -0.143 V, with a positive shift towards less cathodic potentials of almost 20 mV (with respect to the onset that characterizes the O_2 reduction peak of the B,N-GOQDs). The Koutecky-Levich linear fittings (Figure 9.f) obtained from the RDE measurements at different rotation rates (Figure 9.e) provide an average *n* value, over the potential range from -0.5 V to -1.1 V (see Table 3), of 3.71. This is in line with the results discussed above regarding the single B- and N-doping.

Table 3. Potential onsets (derived by the tangent method), peak potentials and number of electrons exchanged during the reduction of oxygen (at different potential values) for the as-prepared systems and after chemical reduction.

	Onset (V)	E_p (V) [a]	*n* (E, V) [a]							
			-0.3	**-0.4**	**-0.5**	**-0.6**	**-0.7**	**-0.9**	**-1.1**	**-1.3**
GOQDs	-0.311	-0.497	-	-	2.21	-	2.23	2.24	2.23	2.22
B-GOQDs	-0.194	-0.456	-	-	2.31	-	2.35	2.28	2.26	2.30
N-GOQDs	-0.198	-0.443	-	-	2.28	-	2.27	2.24	2.23	-
B,N-GOQDs	-0.162	-0.374	-	-	2.50	-	2.49	2.48	2.62	-
red-B-GOQDs	-0.169	-0.366	-	3.47	3.61	3.69	3.82	-	-	-
red-N-GOQDs	-0.179	-0.354	-	2.86	3.36	3.42	3.78	-	-	-
red-B,N-GOQDs	-0.143	-0.316	-	-	3.87	-	3.91	3.92	3.94	-

[a] All the potentials are vs. $Ag/AgCl/Cl^-_{(sat.)}$. The values are calculated for a potential scan rate of 10 mV/s.

3.4 Theoretical modeling

We have designed a number of *local* models for the ORR active sites for both oxidized and reduced doped and co-doped GQDs, based on the characterization data presented in the paragraph 3.2. They are based on a circumcoronene molecule where oxygen, boron and nitrogen atoms are introduced to mimic locally the active sites. The most relevant ones, which will be discussed in the following, are presented by their atomic-spheres representation in Figure 10. We consider three categories of doped species:

a) *Oxidized*. For the B-doped systems, we propose a model with a bioxygenated boron (-BO_2) at the edge of the circumcoronene ($B_{edge}O_2G$), whereas for the B,N co-doped systems, we propose the analogous model with a next-neighbor edge pyridinic N ($B_{edge}O_2GN_{edge}$).;

b) *partially reduced.* For the B-doped systems, we propose a model with an oxygenated boron (-BO) at the edge of the circumcoronene ($B_{edge}OG$), whereas for the B,N co-doped systems, we propose a singly oxygenated species with bonded B-N atoms ($OB_{edge}N_{edge}G$);

c) *fully reduced*. For the B-doped systems, we propose a model with a three-coordinated boron (B-Csp^2) in the central hexagon of the circumcoronene ($B_{bulk}G$), whereas for the B,N co-doped systems, we propose the analogous model with an additional pyridinic N at the edge of the circumcoronene model [27] ($B_{bulk}GN_{edge}$).

The fully reduced B-doped system ($B_{bulk}G$) has been the object of a previous very detailed study, which we refer to for further details in the methodology and approach.[89]

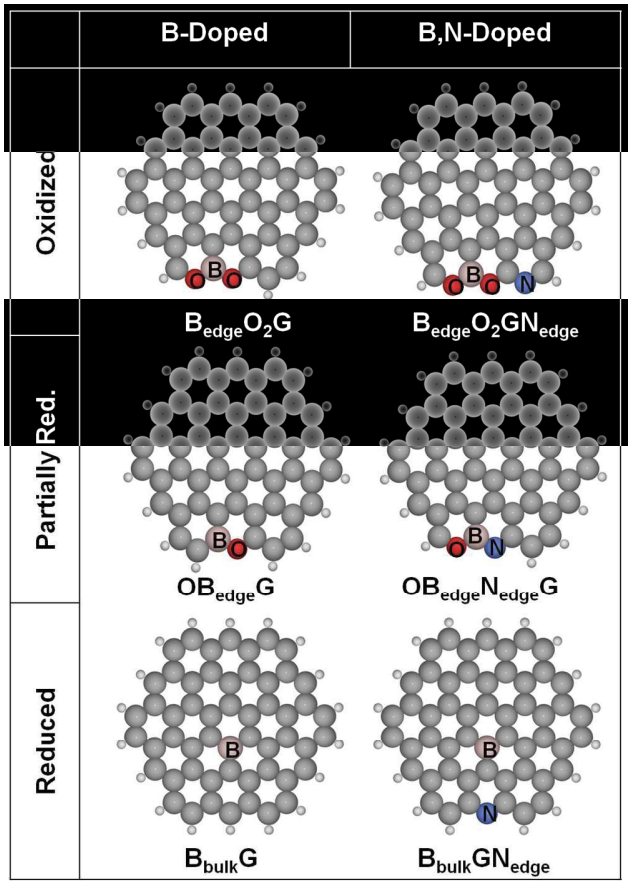

Figure 10. Atomic spheres representation of oxidized, partially and fully reduced B- and B,N-GOQD models considered in this work.

As a next step, for each of these model species of GQDs, we have determined the reaction intermediates and products of the ORR in alkaline solution, according to the associative reaction path (* = active surface site) for the full $4e^-$ process (see also Figure 4):

$$O_{2(g)} + * \rightarrow *O_2 \quad (1)$$

$$*O_2 + H_2O + e^- \rightarrow *OOH + OH^- \quad (2)$$

$$*OOH + OH^- + e^- \rightarrow *O + 2\ OH^- \quad (3)$$

$$*O + H_2O + 2\ OH^- + e^- \rightarrow *OH + 3\ OH^- \quad (4)$$

$$*OH + 3\ OH^- + e^- \rightarrow * + 4\ OH^- \quad (5)$$

This was shown to be favored with respect to the dissociative one in our previous work,[89] as a consequence of the highly demanding steps for the O-O bond dissociation.

The first step of the reaction is the chemical adsorption of the O_2 molecule, which is not observed on undoped reduced QDs (pure circumcoronene). For all the doped models presented above, the O_2 molecule preferentially adsorbs on the positively charged B atom (established by computing NBO charges).

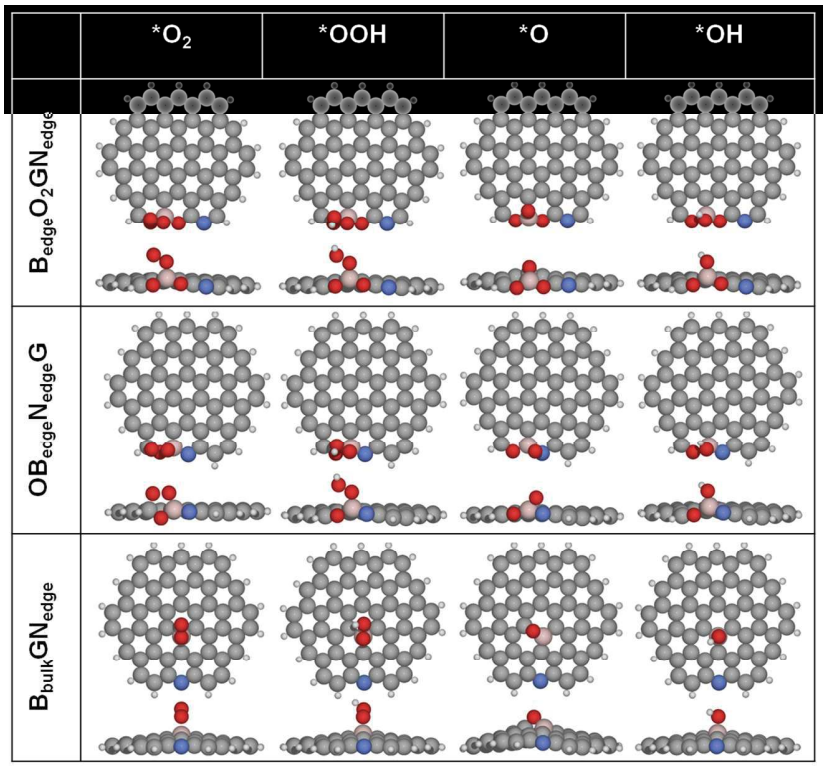

Figure 11. Atomic spheres representation of the ORR intermediates (top and side views) for the oxidized, partially and fully reduced B,N-GOQD models along the associative reaction path. The symbol * is used to represent the surface active site. For the spheres color assignment to atomic species refer to Figure 10.

In Figure 11 we show all the intermediates for the B,N co-doped circumcoronene models in terms of their atomic-spheres representation. The corresponding structures for the B-doped QDs are not shown since they are essentially analogous. These representations clearly highlight that the chemisorption of oxygen containing species (O_2, OOH, O, OH) causes some structural distortion of the systems with the B atom coming out of the QD plane. The most distorted species is *O on the reduced B,N codoped QD ($B_{bulk}GN_{edge}$). It is interesting to note that the -BO_2 and OBN fragments ($B_{edge}O_2GN_{edge}$ and $OB_{edge}N_{edge}G$) are well capable of binding a third or second O atom, since the B atom is a highly positive and, thus, acidic site. It is evident that the chemical nature of the intermediates (*O_2, *OOH, *O and *OH) for the oxidized and reduced QDs is very different. This is expected to have a strong effect on their relative stability with respect to reactants and products of the ORR.

In order to analyze this aspect in further detail we have resorted to the methodology developed by Nørskov and co. [43] for the ORR electrocatalysis by metal surfaces. This approach is based on the construction of free energy diagrams of reactants, intermediates and products along the ORR reaction path, setting the free energy reference level at the value of the reaction products (* + 4 OH^-, for the 4e^- path in alkaline conditions). Additionally, within this methodology it is possible to consider the effect of an applied external bias U by shifting the free energy of each reduction step by $-eU$, where U is the electrode potential and e is the elementary charge. The value of U = -0.5 V (vs Ag/AgCl/$Cl^-_{(sat)}$) was chosen to resemble one of the investigated experimental potentials, as reported in Table 3, so that a direct link between the theoretical outcomes and the experimental observations exists. By applying this bias and the correction for a pH value of 13 (see the computational details in Section 2), we obtain the diagrams in Figure 12.The attention is first focused on the 4e^- path, whose diagrams are reported on the left side of each panel (black line). At a first glance it is evident that the reaction energy profile for the oxidized species, of both B (a) and B,N (b) doped QDs, is very different from the corresponding reduced QDs (left side of panels (c) to (f)). Note that the degree of reduction has a very small influence on the profile of the 4e^- path, thus the left panels of (c) and (d) are very similar to the corresponding left panels (e) and (f). For all reduced species we observe a downhill profile along the four reduction steps with a very large free energy gain (highlighted by blue arrows) associated to the second step, which reduces *OOH to *O, through the release of OH^- in solution.

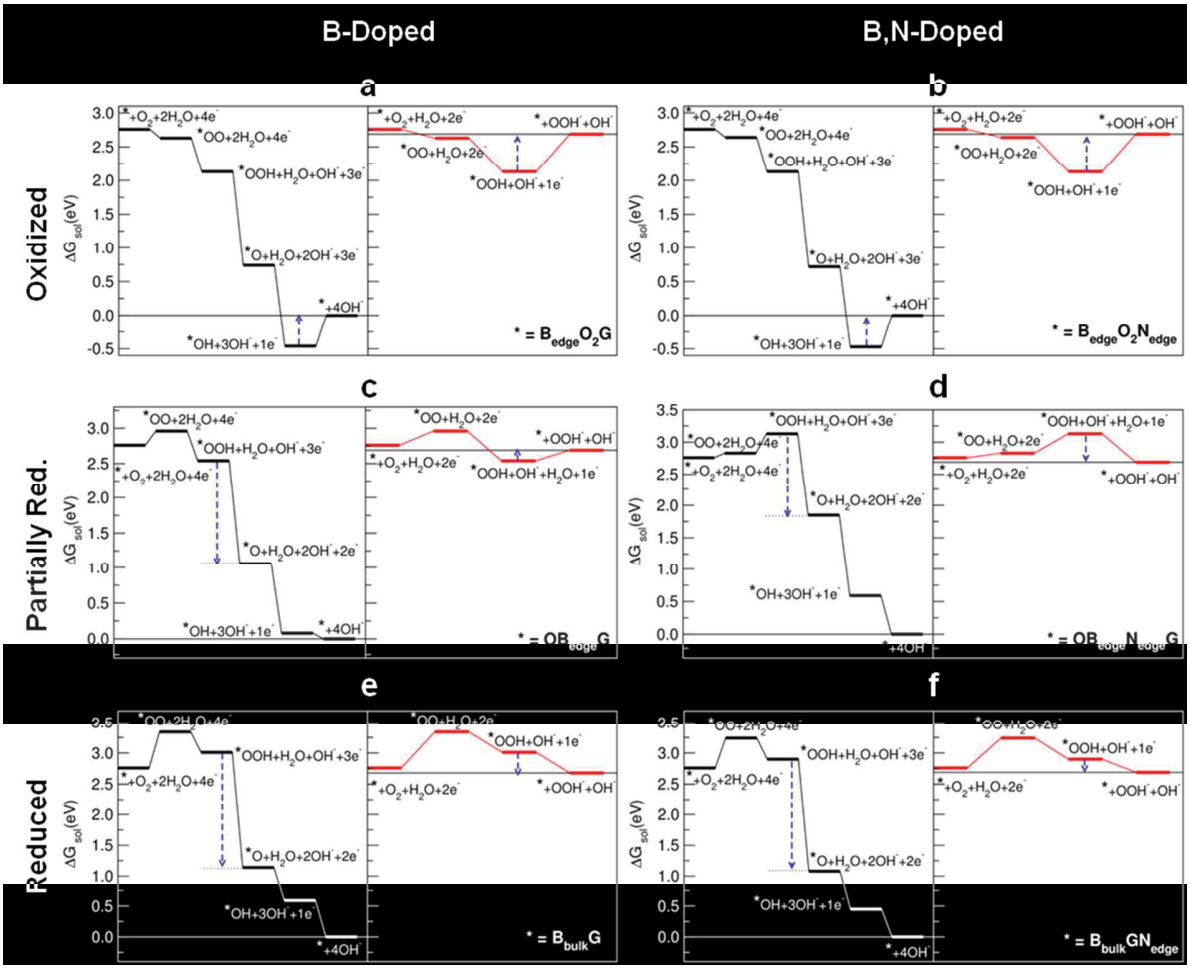

Figure 12. Free energy reaction profiles for the $4e^-$ (black line) and $2e^-$ (red line) pathways of the ORR reaction in aqueous solution (pH = 13) at an external applied potential U = -0.5 V vs $Ag/AgCl/Cl^-_{(sat)}$, as catalyzed by B- or B,N-GOQD models in Figure 10. Blue dotted arrows indicate the most relevant reaction steps determining the $4e^-/2e^-$ selectivity, as discussed in the text.

Differently, for the oxidized species of both B and B,N doped models, the free energy profiles of the $4e^-$ path are not a cascade, since the last reduction step, involving the release of the last OH^-, is an uphill process (see blue arrows in left panels (a) and (b)). This is the major and critical difference between oxidized and reduced models.

Then, we analyze the $2e^-$ path, which consists of the following steps:

$$O_{2(g)} + * \rightarrow *O_2 \quad (6)$$

$$*O_2 + H_2O + e^- \rightarrow *OOH + OH^- \quad (7)$$

$$*OOH + OH^- + e^- \rightarrow * + OOH^- + OH^- \quad (8)$$

The oxygen adsorption (6) and the first reduction step (7), forming *OOH, are the same as for the $4e^-$ path, (1) and (2). On the other hand, the second reduction step along the $2e^-$ path leads to the release

of a hydroperoxide species (OOH^-) in solution and can be competitive with step (3) of the $4e^-$ path where the O-O bond in *OOH is broken, releasing OH^- in solution and leaving *O on the surface

The free energy diagrams of the $2e^-$ paths are reported on the right side of each panel (red line). In the case of the fully reduced species (panels (e) and (f)), the two reduction steps are characterized by a downhill profile. However, the energy gain for the second reduction step, releasing OOH^- species in solution, is definitely much smaller than the second reduction step for the corresponding $4e^-$ path. For this reason we can safely conclude that in the case of fully reduced species, the $4e^-$ path is favored with respect to the $2e^-$ one, in line with the experimental finding reported in the previous paragraph. Differently, in the case of oxidized species (panels (a) and (b)), the last reduction step, for both the $2e^-$ and $4e^-$ pathways are uphill, and by about the same amount of free energy, therefore we expect that in this case the $2e^-$ path becomes competitive with the $4e^-$ path, again in line with what observed experimentally and discussed in previous paragraphs. Finally, for the partially reduced species (panels (c) and (d)), the free energy profile indicates a preference towards the $4e^-$ path, since the $2e^-$ one is slowed down by a barrier for the second step of reduction in the case of B-doping (right panel (c)), or has a small free energy gain associated to the second step of reduction in the case of B,N codoping (right panel (d)).

4. Conclusion

We have reported a systematic study on the preparation and electrochemical characterization of single and dual doped GOQDs, together with the DFT investigation of a set of models consistent with the photoemission analysis.

From the methodological point of view, the use of GOQDs allowed us to investigate for the first time the most fundamental defects of G materials: functionalized edges.

We demonstrated that oxidized GOQDs are quite efficient for the selective production of H_2O_2 through a bi-electronic reduction of O_2. The introduction of dopants can boost the ORR, in particular the B-N codoped materials show a very low overpotential. In an upcoming paper we will demonstrate that the outstanding H_2O_2 selectivity of the oxidized doped-GOQDs combined with their high activities can be efficiently exploited for water remediation application. On the other hand, the chemical activity of doped GOQD can be selectively tuned in order to follow a 4 e^- reduction path (i.e. direct reduction of O_2 to water) simply by the chemical reduction with $NaBH_4$. This treatment has the effect of eliminating the oxygen species that are responsible for the competitive bi-electronic reaction.

Since we are dealing with GOQDs that are intrinsically semiconductive, the reduction process does not affect significantly the macroscopic electric properties like in micrometric GO sheets, but just locally the functional groups. This is a strong indication that a highly conductive 3D structure is not necessary to achieve a high catalytic activity, whereas the pivotal point is to reduce the number of oxygenated species in order to suppress the $2e^-$ reaction path to hydrogen peroxide. GOQDs therefore emerge as highly versatile nanocatalysts with an incredible potential for the realization of very efficient electroactive systems that differently from 3D materials could be used also for homogeneous catalysis. As a matter of fact, GQDs represent the extreme frontier of G nanotechnology, being single layer and just a few nanometers wide, therefore exposing a huge fraction of highly active edges whose chemical nature can be easily modified to favor a specific functionality.

Acknowledgments

MF acknowledge Fondazione Cariparo for financial support. LC thankfully acknowledges a grant from the PRIN Project "DESCARTES" (Project No. 2010BNZ3F2). We acknowledge also financial support from the Fuel Cell and Hydrogen Initiative - Joint Undertaking (FCH-JU) within the CathCat project under contract No. 303492, by the Italian MIUR through the national grant Futuro in Ricerca 2012 RBFR128BEC “Beyond graphene: tailored C-layers for novel catalytic materials and green chemistry” and by the University of Padova funded project: CPDA128318/12 “Study of the catalytic activity of complex graphene nanoarchitectures from ideal to real conditions”.

References

(1) Agnoli, S.; Granozzi, G. *Surf. Sci.* **2013**, *609,* 1.

(2) Zhu, Y.; Murali, S.; Cai, W.; Li, X.; Suk, J. W.; Potts, J. R.; Ruoff, R. S. *Adv. Mater.* **2010** *22,* 3906.

(3) Mkhoyan, K. A.; Contryman, A. W.; Silcox, J.; Stewart, D. A.; Eda, G.; Mattevi, C.; Miller, S.; Chhowalla, M. *Nano Lett.* **2009**, *9,* 1058.

(4) Yamaguchi, H.; Eda, G.; Mattevi, C.; Kim, H.; Chhowalla, M. *ACS Nano* **2010**, *4,* 524.

(5) Wang, H.; Maiyalagan T.; Wang, X. *ACS Catal.*, **2012**, *2*, 781

(6) Wang, X.; Li, X.; Zhang, L.; Yoon, Y.; Weber, P. K.; Wang, H.; Guo, J.; Dai, H.. *Science* **2009**, *324,* 768.

(7) Shao, Y.; Zhang, S.; Engelhard, M. H.; Guosheng, L.; Guocheng, S.; Wang, Y.; Liu, J.; Aksay, I. A.; Lin, Y. *J. Mater. Chem.* **2010**, *20,* 7491.

(8) Qu, L.; Liu, Y.; Baek, J.-B.; Dai, L. *ACS Nano* **2010**, *4,* 1321.

(9) Jin, Z.; Yao, J.; Kittrell, C.; Tour, J. M. *ACS Nano* **2011**, *5,* 4112.

(10) Usachov, D.; Vilkov, O.; Gruneis, A.; Haberer, D.; Fedorov, A.; Adamchuk, V. K.; Preobrajenski, A. B.; Dudin, P.; Barinov, A.; Oehzelt, M.; Laubschat, C.; Vyalikh, D. V. *Nano Lett.* **2011**, *11,* 5401.

(11) Sun, Z.; Yan, Z.; Yao, J.; Beitler, E.; Zhu, Y.; Tour, J. M. *Nature* **2010**, *468,* 549.

(12) Deng, D.; Xiulian Pan, X.; Yu, L.; Cui, Y.; Jiang, Y.; Qi, J.; Li, W.-X.; Fu, Q.; Ma, X.; Xue, Q.; Sun, G.; Bao X.; *Chem. Mater.*, **2011**, *23*, 1188.

(13) Sheng, Z. H.; Shao, L.; Chen, J.-J.; Bao, W.-J.; Wang, F.-B.; Xia, X.-H. *ACS Nano* **2011,** *5,* 4350.

(14) Choi, C. H.; Chung, M. W.; Kwon H. C.; Park, S. H.; Woo, S. I. B. *J. Mater. Chem. A* **2013**, *1,* 3694.

(15) Paraknowitsch, J. P.; Thomas, A. *Energy Environ. Sci.* **2013**, *6,* 2839.

(16) Xue, Y. et al., *Phys. Chem. Chem. Phys.* **2013**, *15,* 12220.

(17) Yang, Z.; Yao, Z.; Li, G.; Fang, G.; Nie, H.; Liu, Z.; Zhou, X.; Chen, X.; Huang, S. *ACS Nano* **2012**, *6,* 205.

(18) Poh, H. L.; Šimek, P.; Sofer, Z.; Pumera, M.; *ACS Nano*, **2013**, *7*, 5262.

(19) Panchakarla, L. S.; Subrahmanyam, K. S.; Saha, S. K.; Govindaraj, A.; Krishnamurthy, R.; Waghmare, U. V.; Rao, C. N. R. *Adv. Mater.* **2009**, *21,* 4726.

(20) Sheng, Z.-H.; Gao, H.-L.; Bao, W.-J.; Wang, F.-B.; Xia, X.-H. *J. Mater. Chem.* **2012**, *22,* 390.

(21) Lin, T.; Huang, F.; Liang, J.; Wang, Y. *Energy Environ. Sci.* **2011**, *4,* 862.

(22) Cattelan, M.; Agnoli, S.; Favaro, M.; Garoli, D.; Romanato, F.; Meneghetti, M.; Barinov, A.; Dudin, P.; Granozzi, G. *Chem. Mater.* **2013**, *25,* 1490.

(23) Das, S.; Sudhagar, P.; Verma, V.; Song, D.; Ito, E.; Lee, S. Y.; Kang, Y. S.; Choi, W.B. *Adv. Funct. Mater.* **2011**, *21,* 3729.

(24) Shen, B.; Jiangtao Chen, J.; Xingbin Yan X.; Xue, Q.; *RSC Adv.*, **2012**, *2*, 6761.

(25) Wang, S.; Zhang, L.; Xia, Z.; Roy, A.; Chang, D. W.; Baek, J.-B.; Dai, L. *Angew. Chem. Int. Ed.* **2012**, *51,* 4209.

(26) Chang, C. H.; Chung, M. W.; Kwon, H. C.; Park, S.H.; Woo, S.I.; *J. Mater. Chem. A*, **2013**, *1*, 3694**.**

(27) Zheng, Y.; Jiao, Y.; Ge, L.; Jaroniec, M.; Qiao, S. Z. *Angew. Chem. Int. Ed.* **2013**, *52,* 1.

(28) Liang, J. Jiao, Y.; Jaroniec, M.; Qiao, S. Z.; *Angew. Chem. Int. Ed.* **2012**, *51,* 11496

(29) Yang, S.; Zhi, L.; Tang, K.; Feng, X.; Maier, J.; Müllen, K.; *Adv. Funct. Mater.* **2012,** *22,* 3634

(30) Dreyer, R.; Jia, H.-P.; Bielawski, C. W. *Angew. Chem. Int. Ed.* **2010**, *49,* 6813.

(31) Pyun, J. *Angew. Chem. Int. Ed.* **2011**, *50,* 46.

(32) Kairdolf, B. A.; Smith, A. M.; Stokes, T. H.; Wang, M. D.; Young, A. N.; Nie, S. *Annual Rev. Anal. Chem.* **2013**, *6,* 143.

(33) Guo, C. X.; Dong, Y.; Yang, H. B.; Li, C. M. *Adv. Energy Mat.* **2013**, *3,* 997.

(34) Lewotsky, K. *SPIE Newsroom*. DOI: 10.1117/2.2201403.01

(35) Favaro, M.; Agnoli, S.; Cattelan, M.; Moretto, A.; Durante, C.; Leonardi, S.; Kunze-Liebhäuser, J.; Schneider, O.; Gennaro, A.; Granozzi, G. *Carbon* **2014**, *77,* 405.

(36) Hummers, W. S.; Offeman, R. E. *J. Am. Chem. Soc.* **1958**, *80,* 1339.

(37) Marcano, D.; Kosynkin, D. V.; Berlin, J. M.; Sinitskii, A.; Sun, Z.; Slasarev, A.; Alemany, L. B.; Lu, W.; Tour, J. M. *ACS Nano* **2010**, *4,* 4806.

(38) Li, Y.; Hu, Y.; Zhao, Y.; Shi, G.; Deng, L.; Hou, Y.; Qu, L. *Adv. Mater.* **2011**, *23,* 776.

(39) Liu, Y.; Wu, P. *ACS Appl. Mater. Interfaces* **2013**, *5,* 3362.

(40) Gaussian 09, Revision D.01, Frisch, M. J.; Trucks, G. W.; Schlegel, H. B.; Scuseria, G. E.; Robb, M. A.; Cheeseman, J. R.; Scalmani, G.; Barone, V.; Mennucci, B.; Petersson, G. A. et al. Gaussian, Inc., Wallingford CT, **2009**.

(41) Becke, A. D. *J. Chem. Phys.* **1993**, *98,* 5648.

(42) Lee, C.; Yang, W.; Parr, R. G. *Phys. Rev. B* **1988**, *37,* 785.

(43) Nørskov, J. K.; Rossmeisl, J.; Logadottir, A.; Lindqvist, L.; Kitchin, J. R.; Bligaard, T.; Jonsson, H. *J. Phys. Chem. B* **2004**, *108,* 17886.

(44) Tomasi, J.; Mennucci, B.; Cammi, R. *Chem. Rev.* **2005**, *105*, 2999.

(45) Marenich, A. V.; Cramer, C. J.; Truhlar, D. G. *J. Phys. Chem. B* **2009**, *113,* 6378.

(46) Li, Y.; Zhao, Y.; Cheng, H.; Hu, Y.; Shi, G.; Dai, L.; Qu, L. *J. Am. Chem. Soc.* **2012**, *134,* 15.

(47) Li, C.-J.; Chen, L. *Chem. Soc. Rev.* **2006**, *35***,** 68.

(48) Fan, Z.; Li, Y.; Li, X.; Fan, L.; Zhou, S.; Fang, D.; Yang, S. *Carbon*, **2014,** *70*, 149.

(49) Lu , J.; Yang, J.-X.; Wang, J.; Lim, A.; Wang, S.; Loh, K. P. *ACS Nano*, **2009**, *3*, 2367

(50) Sun, T.; Fabris, S. *Nano Lett.* **2012**, *12,* 17.

(51) Li, Z.; Zhang, W.; Juo, Y.; Yang, J.; Hou, J. G. *J. Am. Chem. Soc.* **2009**, *131,* 6320.

(52) Li, L.; Wu, G.; Yang, G.; Peng, J.; Zhao, J.; Zhu, J.-J. *Nanoscale* **2013**, *5,* 4015.

(53) Daems, N.; Sheng, X.; Vankelecom, I. F. J.; Pescarmona, P. P. *J. Mater. Chem. A* **2014**, *2***,** 4085; Yang, Z.; Nie, H.; Chen, X.; Chen, X.; Huang, S. *J. Power Sources* **2013**, *236,* 238.

(54) Qu, D.; Zheng, M.; Du, P.; Zhou, Y.; Zhang, L.; Li, D.; Tan, H.; Zhao, Z.; Xie, Z.; Sun, Z. *Nanoscale* **2013**, *5,* 12272.

(55) Favaro, M.; Agnoli, S.; Di Valentin, C.; Mattevi, C.; Cattelan, M.; Artiglia, L.; Magnano, E.; Bondino, F.; Nappini, S.; Granozzi, G. *Carbon* **2014**, *68,* 319.

(56) Dong, Y.; Pang, H.; Yang, H. B.; Guo, C.; Shao, J.; Chi, Y.; Li, C. M.; Yu, T. *Angew. Chem. Int. Ed.* **2013**, *52,* 7800.

(57) Sheng, Z. H.; Shao, L.; Chen, J.-J.; Bao, W. J.; Wang, F. B.; Xia, X.-H. *ACS Nano* **2011**, *5,* 4350.

(58) Sharifi, T.; Hu, G.; Jia, X.; Wågberg, T. *ACS Nano* **2012**, *6,* 8904.

(59) Lai, L.; Potts, J. R.; Zhan, D.; Wang, L.; Poh, C. K.; Tang, C.; Gong, H.; Shen, Z.; Lin, J.; Ruoff, R. S. *Energy Environ. Sci.* **2012**, *5,* 7936.

(60) Wu, G.; Zelenay, P. *Acc. Chem. Res.* **2013**, *46,* 1878.

(61) Jin, J.; Pan, F.; Jiang, L.; Fu, X.; Liang, A.; Wei, Z.; Zhang, J.; Sun, G. *ACS Nano* **2014**, *8*, 3313.

(62) Preobrajenski, A. B.; Vinogradov, A. S.; Mårtensson, N. *Surf. Sci.* **2005**, *582,* 21.

(63) Xing, T.; Zheng, Y.; Li, L. H.; Cowie, B. C. C.; Gunzelmann, D.; Qiao, S. Z.; Huang, S.; Chen, Y. *ACS Nano*, **2014**, *8*, 6856.

(64) Wong, W. Y.; Daud, W. R. W.; Mohamad, A. B.; Kadhum, A. A. H.; Loh, K. S.; Majlan, E. H. *Intern. J. Hydrogen Energ.* **2013**, *38,* 9370.

(65) Hunt, A.; Dikin, D.; Kurmaev, E.; Lee, Y.; Luan, N.; Chang, G.; Moewes, A. *Carbon* **2014**, *66,* 539.

(66) Kobayashi, Y.; Fukui, K.; Enoki, T.; Kusakabe, K.; Kaburagi, Y. *Phys. Rev. B* **2005**, *71,* 193406.

(67) Geim, A.; Novoselov, K. *Nat. Mater.* **2007**, *6,* 183.

(68) Pang, D.; Zhang, J.; Li, Z.; Wu, M. *Adv. Mater.* **2010**, *22,* 734.

(69) Ritter, K.; Lyding, J. *Nat. Mater.* **2009**, *8,* 235; Tapasztó, L.; Dobrik, G.; Lambin, P.; Biró, L. *Nat. Nanotech.* **2008**, 3, 397.

(70) Zhang, Z.; Zhang, J.; Chen, N.; Qu, L. *Energy Environ. Sci.* **2012**, *5,* 8869.

(71) Jeon, I.-Y.; Choi H.-J.; Jung, S.-M.; Seo, J.-M.; Kim, M.-J.; Dai, L.; Baek, J.-B. *J. Am. Chem. Soc*. **2013**, *135*, 1386.

(72) Jeon, I.-Y.; Zhang, S.; Zhang, L.; Choi, H.-J.; Seo, J.-M., Xia, Z.; Dai, L.; Baek, J.-B. *Adv. Mater*. **2013**, *25*, 6138.

(73) Choi, C. H.; Park, S. H.; Woo, S. I. *ACS Nano* **2012**, *6,* 7084.

(74) Ozaki, J.-I.; Kimura, N.; Anahara, T.; Oya, A. *Carbon* **2007**, *45,* 1847.

(75) Wu, Z.-S.; Winter, A.; Chen, L.; Sun, Y.; Turchanin, A.; Feng, X.; Müllen, K. *Adv. Mater.* **2012**, *24,* 5130.

(76) Dai, L. *Acc. Chem. Res.* **2013**, *46*, 31.

(77) Li, Q.; Zhang, S.; Dai, L.; Li, L.-S. *J. Am. Chem. Soc.* **2012**, *134,* 18932.

(78) Strelko, V. V; Kartel, N. T.; Dukhno, I. N.; Kuts, V. S.; Clarkson, R. B.; Odintsov, B. M. *Surf. Sci.* **2004**, *548,* 281.

(79) Jiao, Y.; Zheng, Y.; Jaroniek, M.; Qiao, S. Z. *J. Am. Chem Soc.* **2014**, *136,* 4394.

(80) Mauritz, K. A.; Moore, R. B. *Chem. Rev.* **2004**, *104,* 4535.

(81) Yang, L.; Jiang, S.; Zhao, Y.; Zhu, L.; Chen, S.; Wang, X.; Wu, Q.; Ma, J.; Ma, Y.; Hu, Z. *Angew. Chem. Int. Ed.* **2011**, *50,* 7132.

(82) Ferrighi, L.; Datteo, M.; Di Valentin, C. *J. Phys. Chem. C* **2014**, *118,* 223.

(83) Favaro, M.; Perini, L.; Agnoli, S.; Durante, C.; Granozzi, G.; Gennaro, A. *Electrochim. Acta* **2013**, *88,* 477.

(84) Terrones, M.; Ajayan, P. M.; Banhart, F.; Blase, X.; Carroll, D. L.; Charlier, J. C. *Appl. Phys. A-Mater. Sci. Process.* **2002**, *74,* 355.

(85) Deng, D. H.; Pan, X. L.; Yu, L. A.; Cui, Y.; Jiang, Y. P.; Qi, J.; Li, W. X.; Fu, Q. A.; Ma, X. C.; Xue, Q. K.; Sun, G. Q.; Bao, X. H. *Chem. Mater.* **2011**, *23,* 1188.

(86) Wang, S.; Yu, D.; Dai, L.; Chang, D. W.; Baek, J.-B. *ACS Nano* **2011**, *5,* 6202.

(87) Levich, V. G. Physicochemical hydrodynamics, 2nd ed., Prentice-Hall, 1962.

(88) Wang, D. W.; Su, D. *Energy Environ. Sci.* **2014**, *7,* 576.

(89) Fazio, G.; Ferrighi, L.; Di Valentin C. *J. Catalysis*, *in press*.